



Detection of ionospheric disturbances with a sparse GNSS network in simulated near-real time Mw 7.8 and Mw 7.5 Kahramanmaraş earthquake sequence

F. Luhrmann¹ · J. Park¹ · W.-K. Wong¹ · L. Martire² · S. Krishnamoorthy² · A. Komjáthy²

Received: 29 March 2024 / Accepted: 21 December 2024 / Published online: 18 January 2025
© The Author(s) 2025, corrected publication 2025

Abstract

On February 6, 2023 the Kahramanmaraş Earthquake Sequence caused significant ground shaking and catastrophic losses across south-central Türkiye and northwest Syria. These seismic events produced ionospheric perturbations detectable in Global Navigation Satellite System (GNSS) total electron content (TEC) measurements. This work aims to develop and incorporate a near-real-time (NRT) ionospheric disturbance detection method into JPL's GUARDIAN system. Our method uses a Long Short-Term Memory (LSTM) neural network to detect anomalous ionospheric behavior, such as co-seismic ionospheric disturbances among others. Our method detected an anomalous signature after the second M_w 7.5 earthquake at 10:24:48 UTC (13:24 local time) but did not alert after the first M_w 7.8 earthquake at 01:17:34 UTC (04:17 local time), which had a visible disturbance of smaller amplitude likely due to lower ionization levels at night and potentially the multi-source mechanism of the slip.

Plain Language Summary Seismic activity, including the destructive Kahramanmaraş Earthquake Sequence on February 6, 2023 in the Republic of Türkiye, result in vertical ground displacement that cause atmospheric waves. These waves propagate upwards to the outer atmosphere, disturbing the ionospheric electron content. This disturbance impacts the signals broadcast by positioning satellites (such as GPS) and received by ground-based receivers. If the receiver position is known, the impact to these signals can be used to measure the electron density disturbance caused by these seismically-induced atmospheric waves. Such studies usually rely on being aware of the event a priori. Using deep learning neural networks, we instead aim to detect anomalous signals automatically. We propose to utilise this method to detect seismically-induced disturbances over a large geographical area. The detection method proposed in this paper successfully detected an anomalous event in the ionosphere approximately ten minutes after the second earthquake in the Kahramanmaraş Earthquake Sequence.

Keywords Ionosphere · Ionospheric anomaly detection · Deep learning · Co-seismic ionospheric disturbance · GNSS

Introduction The East Anatolian Fault Zone (EAFZ) in the Republic of Türkiye has produced fewer earthquakes relative to the North Anatolian Fault Zone (NAFZ) in the last 200 years. Therefore, with increasing seismic potential, it was anticipated to produce severe earthquakes in the region (Gokceoglu 2023). On February 6, 2023 01:17:34 UTC (04:17 local time) a M_w 7.8 earthquake with a strike-slip

mechanism hit, consistent with the EAFZ location and orientation, west of Pazarcık (Goldberg et al. 2023). Nine hours later at 10:24:48 UTC (14:24 local time) a M_w 7.5 earthquake, to the north of the first earthquake and south of Elbistan, struck. These successive earthquakes, known as the Kahramanmaraş Earthquake Sequence, resulted in a tragic death toll over 50,000, with 13 million people across 11 provinces directly affected (Gokceoglu 2023).

The ionosphere is composed of free ions and electrons at the earth's outermost atmospheric layer, beginning approximately at 80 km altitude. Changes in the ionosphere's total electron content (TEC) can be observed with ground-based Global Navigation Satellite System (GNSS) receivers (Calais and Minster 1995; Afraimovich et al. 2001). Earthquakes and ground explosions, such as the Kahramanmaraş

✉ F. Luhrmann
luhrmanf@oregonstate.edu

¹ College of Engineering, Oregon State University, 101 Covell Hall, Corvallis, OR 97331-2409, USA

² Jet Propulsion Laboratory, California Institute of Technology, 4800 Oak Grove Drive, Pasadena, CA 91109, USA

Earthquake Sequence, generate acoustic pressure waves that propagate vertically and displace the electron density profile of the ionosphere with the same frequency as the atmospheric wave (Kotsarenko et al. 1997). Kherani et al. (2009) studied this coupling mechanism with acoustic wave momentum transfer and confirmed that atmospheric waves, such as ones generated by seismic events, are the driving force of electron density fluctuations primarily in the F region of the ionosphere and therefore observed in GNSS observations. A survey of over 700 seismic events with $M_w > 5$ by Zaslavski et al. (1998) concluded that TEC measurements can be used to monitor these seismically induced ionospheric disturbances.

Extensive studies have used GNSS receivers to measure TEC and observe TIDs induced by earthquake events such as Occhipinti et al. (2013), DasGupta et al. (2006), Rolland et al. (2011) and Sanchez et al. (2022). Fewer studies have attempted to implement an ionospheric disturbance detection method capable of detecting ionospheric disturbances induced by acoustic waves originating from earthquake events. An early study by Lin (2012) unsuccessfully attempted to detect ionospheric disturbances using nonlinear principal component analysis after the January 1, 2012 (UTC) earthquake at Japan's Izu Islands. Akhoondzadeh (2013) tested a multilayer perceptron model to detect ionospheric anomalous behavior induced by the Tohoku earthquake of March 11, 2011 (UTC), but was not successful in detection. A recent study tested a deep learning based ionospheric anomaly detection method (Muhammad and Külahçı 2022) using an encoder-decoder Long Short-Term Memory (LSTM) neural network architecture to detect anomalous ionospheric behavior during geomagnetic storms and after earthquake events. Although able to detect geomagnetic-solar disturbances, Muhammad and Külahçı (2022) acknowledged the inability to detect earthquake induced ionospheric anomalies after a $M_w 7.4$ earthquake in Oaxaca, Mexico on June 23, 2020.

Recent studies have shown success with machine learning algorithms in discriminating events of interest using supervised methods requiring labeled training data. Liu and Morton (2020, 2022) improved detection of satellite oscillator anomalies with machine learning methods over previous studies. In the area of seismic ionospheric disturbances, Brissaud and Astafyeva (2022) have shown successful use of a supervised Random Forest algorithm in discriminating between co-seismic ionospheric disturbances and noise in post-processed TEC measurements. Brissaud and Astafyeva (2022) trained their model on a class-balanced, labeled dataset of 2867 co-seismic ionospheric disturbance TEC measurements over 12 earthquake events and tested their model's success on different TEC measurements from these 12 events. Constantinou et al. (2023) showed success with supervised

Convolutional Neural Network classification of images representing TEC values of a 60-minute window. This method classifies the image as anomalous, trained with images containing tsunami-induced ionospheric disturbances. Although these previous studies have shown success with ionospheric disturbance classification, our goal is to remove the need for an extensive labeled dataset of historic ionospheric observations and instead provide a detection tool capable of identifying anomalies without labeled training data using only TEC values as input.

Recently, the GNSS-based Upper Atmospheric Realtime Disaster Information and Alert Network (GUARDIAN) became an operational research tool (Martire et al. 2022). The GUARDIAN system ingests streaming data from approximately 90 stations worldwide and provides multi-GNSS near real-time (NRT) TEC observations for exploration by the general public and scientific community (guardian.jpl.nasa.gov). The GUARDIAN NRT TEC stream can, in principle, be used for hazard monitoring and warning using the ionosphere in the event of earthquakes, tsunamis, geomagnetic storms or other natural and anthropogenic events. However, with such a large dataset, the problem of timely and efficient anomaly identification is non-trivial. With anomalous ionospheric behavior flagged reliably, contextual information such as earthquake location, USGS tsunami classification, and geomagnetic conditions can help a human operator robustly classify the source of the anomaly - we contend that from an early warning perspective, there is not a substantial inherent advantage to achieving full classification in an autonomous way, as a human operator has to review data before issuing a warning, potentially causing a large-scale evacuation. A bigger challenge in this process is the vast amount of data that a human operator may need to review to find the anomaly. Our process significantly reduces the effort required for this step. In our work, we advance the frontier of real-time detection of ionospheric anomalies by applying the LSTM-based deep learning method to a simulation of the GUARDIAN real-time data-stream, with fresh data supplied to our algorithm in simulated NRT in 10-minute intervals, as they would appear using GUARDIAN (as opposed to post-processed). In this paper we define NRT as under fifteen minutes with the goal of a ten minute detection from time of event. We use the Kahramanmaraş earthquake sequence as a testbed for this approach and demonstrate the feasibility of an LSTM-based anomaly identification network to identify TIDs of interest in an NRT stream. Using an NRT stream generates unique challenges over the use of post-processed data in previous work cited above, as anomalies develop within the time scale of identification. In addition, NRT data can often contain anomalies of nonphysical origin as uncorrected latch-ups, cycle slips and data gaps may exist, which adds another challenge to any identification scheme. To the best of our knowledge, this is the first such

demonstration of real-time anomaly identification in a real-time streaming TEC time series after a geophysical event.

The use of the proposed NRT ionospheric anomaly detection system is intended to be deployed worldwide across the GUARDIAN system. Therefore, the setup of the experiment is done with this end goal in mind. Additionally, the design of the detection algorithm is focused to acoustic and gravity wave generated disturbances and not limited solely to seismic events. Therefore the input for detection will only be the TEC measured data from GUARDIAN. We want to achieve detection with minimal conditions in order to be fully scalable and thus applicable to the GUARDIAN system and other TEC-based NRT streams.

The following sections will cover the Kahramanmaraş earthquake sequence, the regional GNSS ground-based stations used for detection, the ionospheric anomaly detection methodology, including the LSTM development, and lastly the results of anomaly detection over the test dataset, January and February of 2023.

Kahramanmaraş earthquake sequence

The Kahramanmaraş earthquake sequence in southern Republic of Türkiye caused serious damage to buildings, infrastructure, and significant loss of human life, becoming the seventh deadliest earthquake since 1950 worldwide (NGDC & WDS 2023). The first earthquake occurred at 01:17:34 UTC, 04:17 local time when many were inside their homes. Additionally, a winter storm meant exposure to freezing temperatures for those displaced and made homeless from the damage. Both earthquakes caused severe levels

of shaking as far away as 10 km from the ruptures and up to 8 ms of horizontal displacement, leveling buildings in the region and offsetting rail and roadways. Up to 13 million people experienced shaking, including 2.9 million internally displaced population in Syria (Hussain et al. 2023).

The seismic mechanism differed between the two earthquakes in the sequence. The first rupture exhibited four discrete events along 350 km length of fault lines. In contrast, the second rupture was confined to 80 km length due to geometric barriers of the EAFZ, and exhibited one single, continuous event along the faultline (Okuwaki et al. 2023). The second earthquake was described as a relatively focused rupture by Okuwaki et al. (2023). Previous research by Riabova et al. (2023), Maletckii et al. (2023) and Bagiya et al. (2023) has shown the ionospheric disturbance recorded by GNSS for both earthquake events, with the earliest disturbance attributed to the acoustic wave generated by the seismic events. Riabova et al. (2023) notes a gravity wave disturbance recorded at geomagnetic observation sites in the region.

Seven GNSS ground-based stations were chosen for this experiment from the GUARDIAN system (Martire et al. 2022) across the Mediterranean region. These include stations MADR, TLSE, GRAC, MATZ, DYNG, NICO, and BSHM. Satellite constellations used included GPS, Galileo, GLONASS, and BeiDou. See Fig. 1 for the location of these stations and the earthquake epicenters. Based on this configuration, we anticipate detection of the seismically-induced TIDs in station NICO and BSHM TEC measurements.

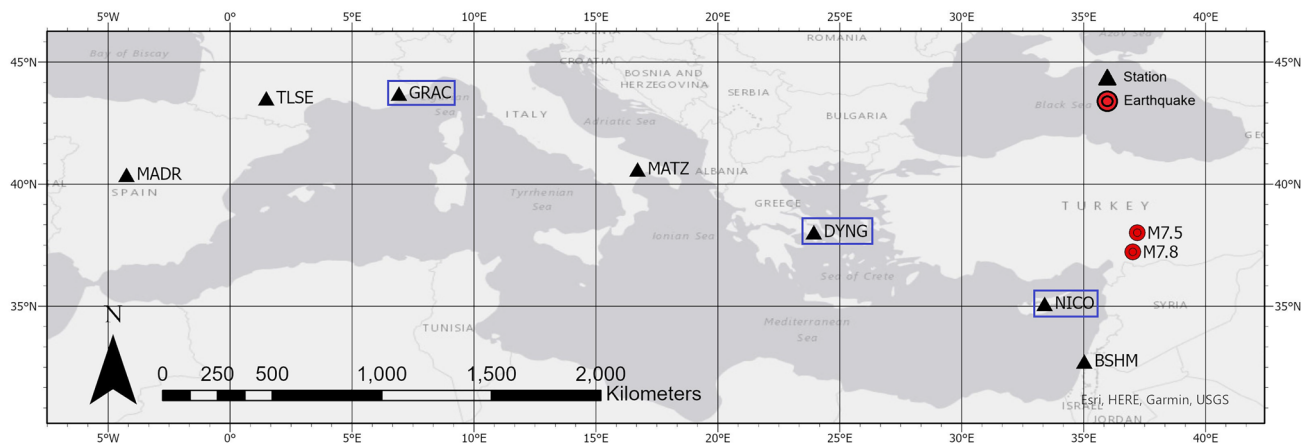


Fig. 1 Map of the GNSS station locations, black triangle, and earthquake epicenters, M_w 7.8 37.226°N 37.014°E and M_w 7.5 38.011°N 37.196°E, red circle. Stations with a blue rectangle are used for training the LSTM models

Ionospheric anomaly detection methodology

Slant TEC, measured in TEC Units ($1 \text{ TECU} = 10^{16} \text{ electrons/m}^2$), is estimated by GUARDIAN with the linear combination of dual-frequency L1 and L2 measurements as detailed in Teunissen and Montenbruck (2017). These values are further processed inside GUARDIAN in real time with a fourth-order Butterworth high-pass filter, removing frequencies below 15 min periods, or approximately 1.1 mHz (Martire et al. 2022). We expect TID disturbances due to gravity waves to range between 1 to 3 mHz, disturbances due to acoustic waves to be approximately greater than or equal to 4 mHz, and overall waves to be less than 10 mHz, based on Matoza et al. (2022). The frequency-filtered slant TEC data is hereafter referred to as dTEC. After GUARDIAN's processing methods, we limited the data to a cutoff elevation of 30° and dTEC absolute values $\leq 3 \text{ TECU}$, in an effort to remove extreme outliers likely due to non-ionospheric behavior. Along with dTEC, GUARDIAN also provides the ionospheric pierce point (IPP) locations of the dTEC values, using a single-shell ionospheric model fixed at 350 km altitude (Martire et al. 2022).

LSTM prediction

An LSTM is a deep learning recurrent neural network architecture, often successful in sequence prediction tasks. These architectures, unlike a standard feed forward network, are cyclical in nature and employ several activation functions stored for each time step in an internal state to the networks cell. Therefore, internal states are not limited to a fixed input window of the time series. Instead the LSTM, using these cell states, have a dynamic contextual window of all previous sequences for prediction of future values (Hochreiter and Schmidhuber 1997; Sak et al. 2014). The specific architecture of the LSTM cell employed for our research can be seen in Sak et al. (2014).

The foundation of the ionospheric anomaly detection method is built on the assumption that the LSTM is able to learn the temporal dynamics of ionospheric dTEC. Therefore when actual dTEC measurements deviate from the predicted values output by the LSTM, this will indicate atypical ionospheric behavior. This method determines what is deemed typical in ionospheric behavior simply by the dTEC data that is used in training the LSTM. Therefore, we assume that the model absorbs the current geomagnetic activity as "typical". For a full-scale deployment of this method, we will need to ensure that the training data used is sufficient across a given time period, e.g. a rolling window of three months, to reflect seasonal geomagnetic behavior changes in the ionosphere as well as exclude or mask events of interest in the training

data, such as co-seismic atmospheric waves. Additionally, we will need to be cognizant of the regional typical behavior and cluster training and testing data accordingly.

The LSTM parameters are chosen using the Ray Tune Hyperparameter Tuning method (Liaw et al. 2018) by minimizing the loss function. Here our loss function is Mean Square Error (MSE). The error measure is the difference between the LSTM prediction of TEC and the ground truth measured value of TEC. Three GNSS ground-based stations were chosen to represent the regional behavior. TEC data from GNSS station GRAC, see Fig. 1, are used to create a LSTM prediction model for GNSS stations GRAC, TLSE, and MADR. TEC data from GNSS station DYNG, see Fig. 1, are used to create a LSTM prediction model for GNSS stations DYNG and MATZ. Finally, TEC data from GNSS station NICO, see Fig. 1, are used to create a LSTM prediction model for GNSS stations NICO and BSHM. For each of these three models we have chosen the satellite GPS SVN 50.

LSTM parameters chosen using the Ray Tune method include LSTM layers, LSTM hidden units, and batch size. The LSTM learning rate is optimized using the ReduceLROnPlateau optimizer, part of the PyTorch library (Paszke et al. 2019). For the MSE results across the different LSTM hyperparameters please see the Supplement Table S2 and Table S3. These results show that different LSTM parameters are optimal for each of the three station models. Overall 2 or less LSTM layers and 256 or less LSTM hidden units are optimal for TEC prediction for this experiment. In order

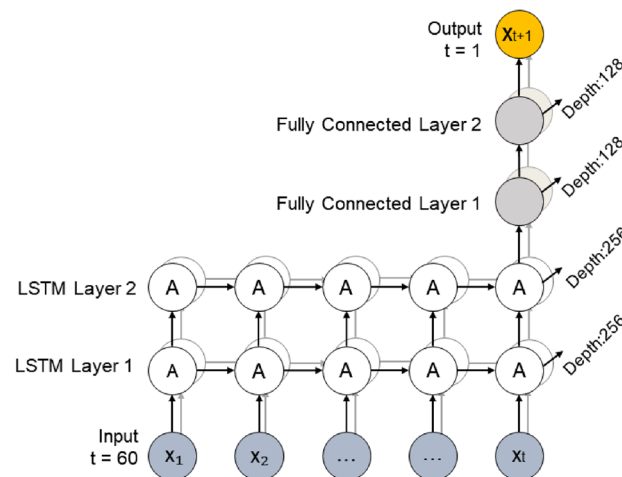


Fig. 2 The chosen LSTM architecture of a two-layer LSTM network with 256 neurons per hidden layer as indicated by the depth metric. 'A' is an LSTM cell with forget gate, see (Sak et al. 2014) for further cell architecture and equations. The LSTM layers are followed by two fully connected layers with 128 neurons per layer as indicated by the respective depth metric. The input is a time series sequence of 60 dTEC measurements, with an output of one predicted dTEC measurement. PyTorch was used for model development (Paszke et al. 2019)

to reduce custom model development, and test a uniform architecture across all stations, the LSTM architecture of 2 layers and 256 hidden units was chosen, See Fig. 2. Training spanned 100 epochs, using the Adam optimization method (Kingma and Ba 2014).

Train and test data sets

Three LSTM models were trained in total. TEC measurements from stations NICO, DYNG, and GRAC paired with satellite GPS SVN 50 were used to train the three LSTM TEC prediction models. Satellite GPS SVN 50 was chosen arbitrarily, but showed beneficial characteristics such as low signal disruption due to loss or cycle-slip during the training data time period. Training data spanned from September 15, 2022 to December 31, 2022 (3.5 months). The LSTM prediction model trained with TEC data from NICO was used on test data from NICO and the nearby station BSHM. The LSTM prediction model trained with TEC data from DYNG was used on test data from DYNG and the nearby station MATZ. The LSTM prediction model trained with TEC data from GRAC was used on test data from GRAC and the nearby stations TLSE and MADR. The training dataset was split into training and validation and tuned on the validation data to minimize the Normalized MSE loss over 100 epochs. Test data spanned from January 1, 2023 to February 28, 2023 (2 months). Test data was never "seen" by the three LSTM models during training and validation. Overall there were 734 station-satellite pair test data that were processed for anomaly detection.

This method was used instead of training a LSTM TEC prediction model for each station and satellite pair to save compute resources. This method tests the ability to scale this approach to a much larger region where training a model per station will be prohibitive. We assume that the distribution, in the statistical sense, of the training data for the three stations NICO, DYNG, GRAC is not sufficiently different from the test data across all stations to warrant domain adaptation techniques. Domain adaptation techniques are often employed in machine learning when the source data and target data distributions differ. Here, an example would be NICO TEC measurements as the source data and BSHM TEC measurements as the target data. An example of a domain adaptation techniques would include the development of a frequency-based encoder model to learn the optimal translation between the source data and target data (He et al. 2023).

In order to mimic a near-real time data stream, we input the test data in 10-min window with 5 min of overlap between each window. The overlap ensures that TID events at the edge of a 10-min window can still be successfully detected in the next round of testing. Data

gaps are identified by tracking time stamps at the end of 10-min window data groups and the length of data within each group. Data groups with missing data (lengths below expected amount based on sample rate) or missing the end time stamp are skipped. We acknowledge that this filter may remove potential ionospheric disturbances from the data set but these efforts are made to minimize false detection which occur due to signal loss.

Error threshold and count

The trained LSTM generates the dTEC predictions for the 10-minute test data set. Square errors are calculated for each time step in the 10-minute test set. The error threshold, α , is set to the training set's MSE, \bar{x} , plus three times the training set's square error sample standard deviation, $3s$, see Eq. (1). If errors exceed the error threshold α then the time step is flagged with value "1". Using the sum across a rolling window of 24 time steps, we calculate a rolling error count using the flagged value "1". If this error count exceeds three, the 10 min data set is passed for further processing in the next detection step.

$$\bar{x} = \frac{1}{N} \sum_{i=1}^N (y_i - \hat{y}_i)^2 s = \sqrt{\frac{\sum(x_i - \bar{x})^2}{n-1}} \quad (1)$$

Within this process we also run a simplified check for cycle-slips in addition to the GUARDIAN data stream cycle-slip detection and amelioration technique called the Adaptive Break Detector (ABD), developed at JPL. After the error count, we take the absolute difference between time t and time $t+1$. If this difference is larger than one ($\Delta t > 1$ TECU), we assume cycle-slip and remove this data set from further testing. This reduced the error triggers from 1092 to 193 before phase synchrony testing, illustrating the potential difficulties in working with near real time data streams in anomaly detection.

Phase synchrony and distance threshold

Data sets flagged from the previous step are processed in a pair-wise manner to calculate phase synchrony measurements. The basis for this filter is that during an atmospheric disturbance, nearby dTEC time series measurements will not only correlate but also come into phase accounting for lag time. Therefore testing for phase synchrony between two time series will detect synchronous wave events in the ionosphere. The phase synchrony measurement is derived from Eq. 2, where φ_{ij} is the phase synchrony between two stations and $h(x_i)$ and $h(x_j)$ are the

Hilbert Transforms of the two station dTEC values. See Supplement Figure S1 for an example illustration of how the measurement results from two cosine waves with different amplitudes and phase shifts, but similar frequencies.

$$\varphi_{ij} = 1 - \sin\left(\frac{|h(x_i) - h(x_j)|}{2}\right) \quad (2)$$

A lag is allowed for in-phase synchrony measures of 5 min between two ten-minute data sets. If the phase synchrony measure exceeds the value of 0.9 the pair-wise data is checked to confirm that synchronous anomalies are within 200 km, IPP distance, of each other. This aids in the removal of false positives and is founded on the belief that TID induced from atmospheric generating events will be somewhat similar over a broad area.

For the combined process flow diagram see Fig. 3.

Results

A full tabulation of results from our ionospheric NRT anomaly detection method across the test data for the two months January 1, 2023 through February 28, 2023 can be seen in Table 1. Overall, there are seven ionospheric anomalies detected, see Fig. 4. From Fig. 5 we see a clear detection after the M_w 7.5 earthquake. The anomaly detection method, which flags the entire 10 min window as an anomaly, picks up the TID approximately starting at 10:34 (UTC), 10 min after the earthquake at 10:24 (UTC). Once a detection occurs, the entire window from 10:29 to 10:39 UTC is highlighted as an anomaly. In total, five signals were identified as anomalous across one station (NICO) closest to the earthquake epicenter, and five satellites across four constellations. This ionospheric disturbance

Table 1 Anomaly detection date time results between January 1 and February 28, 2023

Date YYYY-MM-DD (UTC)	Time (UTC)	Time (Türkiye) (+3)
2023-01-11	13:53:57–14:00:57	16:53:57–17:00:57
2023-01-27	05:02:37–05:10:57	08:02:37–08:10:57
2023-02-01	08:40:37–08:48:57	11:40:37–11:48:57
2023-02-02	11:51:37–11:59:57	14:51:37–14:59:57
2023-02-02	15:32:37–15:39:57	18:32:37–18:39:57
2023-02-06	10:29:37–10:41:57	13:29:37–13:41:57
2023-02-15	16:41:37–16:45:57	19:41:37–19:45:57

exhibits amplitudes of $\sim[-2, 2]$ TECU (Fig. 5), a horizontal propagation velocity of ~ 1.9 km/s (Fig. 7), and maximum frequencies ~ 4 mHz (Fig. 6), which is similar to previously studied co-seismic TID (Occhipinti et al. 2013). Therefore, we are confident that this disturbance is a result of the M_w 7.5 earthquake event. We emphasize here that our ionospheric detection algorithm, searching across seven stations, detected a co-seismic ionospheric disturbance at one of these stations, exhibiting detection from a sparse GNSS network. Other signals, including from station BSHM, show a significant disturbance but were not flagged by the detection algorithm. This is due to the balance between error threshold and error count against number of detections. In this experiment, the threshold for MSE was ± 0.084 TECU, 3x standard deviation from the mean MSE of training data. What is also of note are the other detections shown in Fig. 4 that do not exhibit atmospheric wave behaviors. These detections occur around signal loss events.

When we reference the seven ionospheric anomalies detected, these are what the algorithm has determined as

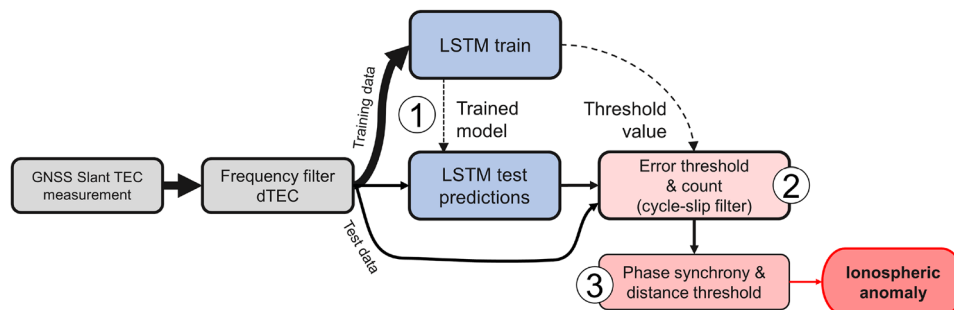


Fig. 3 Process flow diagram for ionospheric anomaly detection methodology. After filtering the TEC data with a high pass filter, the data is split into training and test data sets (1). The LSTM is trained with the training data set. These trained models are frozen and then used to create predictions for the test data set. These predictions are differenced with actual, measured dTEC values and these residual values are then sent to error thresholding and count filtering (2). Residual

values over the error threshold and count are flagged and their time step is also flagged. Time series windows of dTEC values within which these flagged time steps exist are sent to the final filter process, phase synchrony and distance thresholding (3). Time series windows of dTEC values that show high phase synchrony with other, local, flagged signals are finally identified as ionospheric anomalies

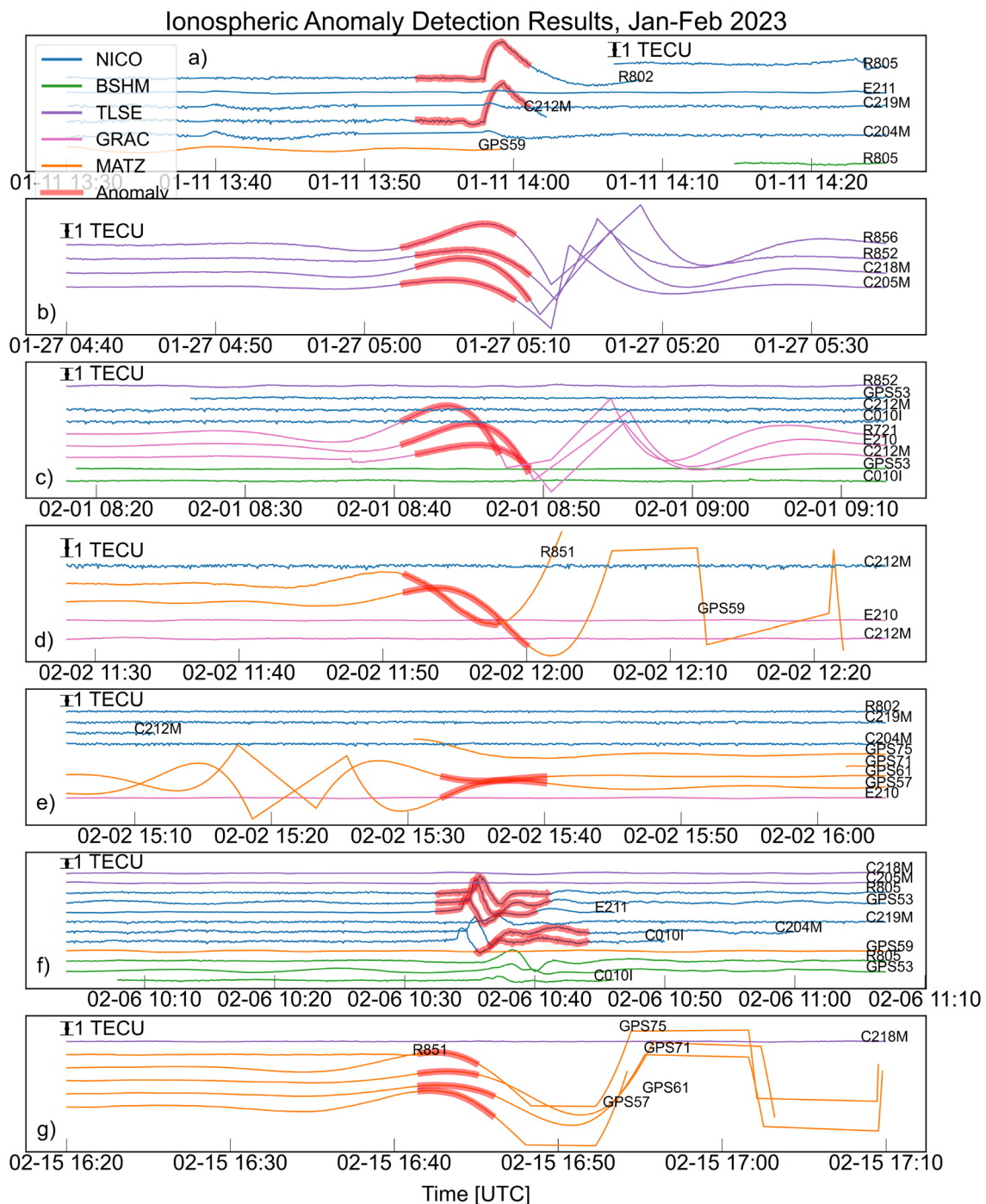
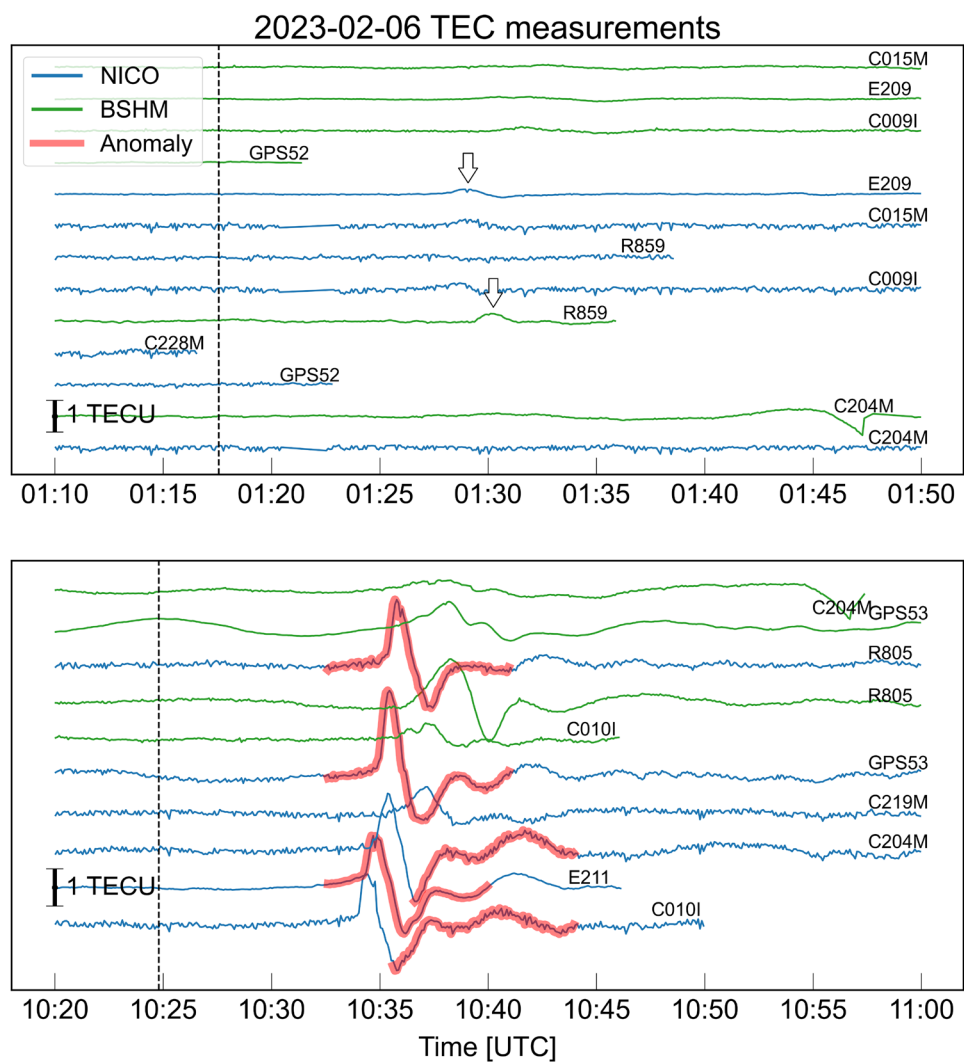


Fig. 4 Detections of potentially anomalous ionospheric behavior. Panel **a** Potential anomalous behavior on 01-11-2023 between 13:50 and 14:05 UTC shown in red at station NICO. There is a clear change in the signal, but other nearby signals do not display a similar pattern. This is likely limited to station NICO. Panel **b** Potential anomalous behavior on 01-27-2023 between 05:00 and 05:15 UTC shown in red at station TLSE. There is no evidence of disturbance during this time period. Panel **c** Potential anomalous behavior on 02-01-2023 between 08:30 and 09:00 UTC shown in red at station GRAC. There is evidence of signal loss at the end of this time period and likely

the cause of the detection. Panels **d**, **e** Potential anomalous behavior on 02-02-2023 between 11:50 and 12:05 UTC and 15:25 and 15:45 UTC shown in red at station MATZ. There is evidence of several signal losses across the hours 12:00 to 16:00 UTC and therefore likely the cause of the detection. Panel **f** The atmospheric wave detection at station NICO 10 min after the M_w 7.5 earthquake. Panel **g** Potential anomalous behavior on 02-15-2023 between 16:40 and 16:50 UTC shown in red at station MATZ. There is evidence of signal losses and therefore likely the cause of the detection

Fig. 5 Top: The ionospheric anomaly detection method did not detect the smaller disturbance after the first M_w 7.8 earthquake event at 01:17 UTC, epicenter 37.226° N 37.014° E. Small disturbances are visible between 01:28 and 01:29 UTC, 11 min after the earthquake, highlighted by the two arrows. Bottom: The ionospheric anomaly detection results after the M_w 7.5 earthquake at 10:24 UTC (vertical dashed line). The x-axis is time in UTC, the y-axis is TEC (TECU) offset in order from bottom to top of distance in kilometers to the M_w 7.5 earthquake epicenter, 38.011° N 37.196° E, with the closest signals at the bottom of the plot. The red indicates the detected ionospheric anomalies. In total there are five station-satellite signal pairs that were flagged for ionospheric anomaly. These include station NICO and satellites C010I, C204M, E211, GPS53, and R805. Therefore, this is a multi-constellation detection event. Detections were not made at similarly large disturbances seen in BSHM-R805, BSHM-GPS53, and NICO-219 M



anomalous behavior. To the trained eye, we can see that the algorithm has determined that several signal losses, and times surrounding signal loss, are anomalous. Therefore, our definition of anomalous here is simple, it is what the algorithm has detected as atypical behavior. Indeed, these signal loss events look atypical in their context, and we argue that detection of short-term signal loss can be advantages to operational monitoring in near real time.

There was no anomalous detection after the M_w 7.8 earthquake earlier in the day, seen in Fig. 5. A small disturbance can be seen at 01:28 UTC at a much lower amplitude than the M_w 7.5 event. Bagiya et al. (2023) has proposed several reasons behind this minimal ionospheric disturbance from the first earthquake. The primary cause is likely the lower ionization levels during night time. At 04:17 local time when the first earthquake hit, we may not be able to detect with our method a seismically induced TID from the ionization in the F-layer alone, although a small disturbance is visible. We note in Supplement Figure S2 that the TEC processed

by GUARDIAN agrees well with post-processed TEC from candidate links, which show the appearance of the TID. The secondary cause that Bagiya et al. (2023) proposes is the slip process, instead of a single source strike-slip event like the later M_w 7.5 earthquake, the M_w 7.8 earthquake showed at least two sources for strike-slip events along the fault. They speculate that the lower amplitude observed in TEC could also be due to interference between two or more acoustic waves produced from the multi-source mechanism of the slip. Based on the findings in Maletckii et al. (2023), which used a different slant TEC detrending method, the TEC time derivative, they show a disturbance at stations NICO and BSHM with satellite E209 with an amplitude of $\approx 0.2\text{--}0.3$ TECU. This shows that detection is dependent on TEC detrending methods used for ionospheric observation.

Closer analysis of the detected anomalous ionospheric behavior from station satellite signals NICO-C010I, NICO-E211, and NICO-GPS53 in Fig. 6 show the acoustic wave frequency. Both NICO-C010I and NICO-E211 signals end

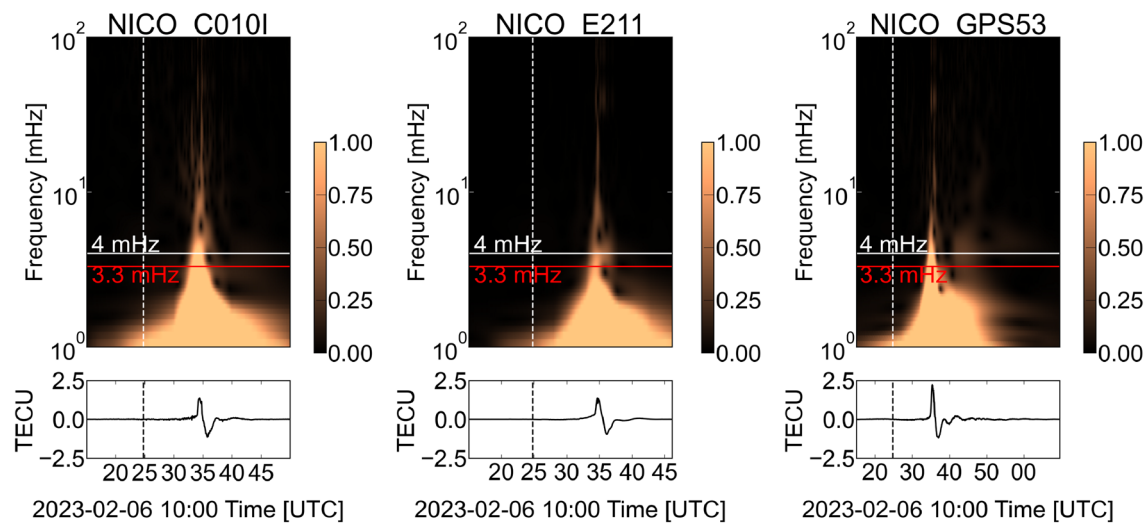


Fig. 6 Continuous Wavelet Transform on the anomalous waveforms detected from 2023-02-06 10:00 to 11:40 UTC with a Hamming window applied to the data. The lowest measure of 1 millihertz (mHz) is due to the high-pass filter, the upper measure of 100 mHz is the top measure capped by the sample rate. The horizontal red dashed line

is the representative acoustic cutoff frequency 3.3 mHz (Srivastava et al. 2021). From these measures we observe the frequency spike to 4 mHz and above. Vertical lines correspond to the time of the earthquake

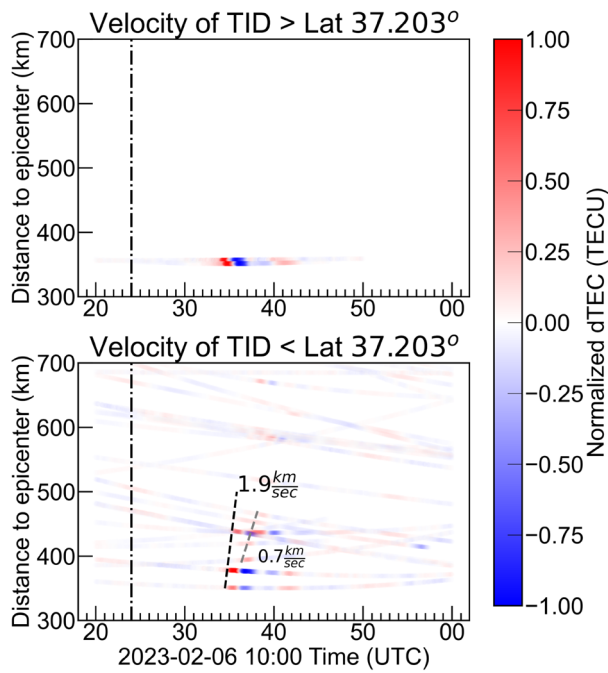


Fig. 7 Top: The disturbance to the north of the earthquake's epicenter is seen in only two signals—this does not allow us to compute a velocity estimate. Bottom: The disturbance to the south of the earthquake's epicenter shows a primary disturbance moving at approximately 1.9 km/s horizontally away from the epicenter, with a secondary, lower amplitude wave moving approximately 0.7 km/s

before 11:00 UTC, but NICO-GPS53 continues showing a more complete picture of the wave propagation. We observe acoustic waves occurring above the 3.3 mHz threshold (red horizontal line), all approximately 10 min after the earthquake event.

In total, we tested 8496 ten-minute windows, not including overlap, between 1 January and 28 February, 2023. Only 0.02% of the data tested, 2 ten-minute windows, contain visible coseismic ionospheric disturbances after the Mw 7.7 and Mw 7.5 earthquakes. Furthermore within each 10-minute window we conservatively estimate that across the 7 stations, approximately 8 satellites would be in view on average per station, providing 56 signals within each 10-min window. In total 475,776 signals processed, of which three after the Mw 7.7 earthquake and 12 after the Mw 7.5 earthquake capture the coseismic ionospheric disturbance, or 0.003% of the total signals tested. Both of these measures illustrate the extreme class imbalance of the positive class for this experiment and the difficulty of successfully identifying an extremely rare event among an extensive and potentially noisy data set. Therefore successful detection of five anomalous signals after the Mw 7.5 earthquake is considered a promising result in an experiment with such extreme class imbalance. Moving forward we will work to improve detection to include the majority of the signals that capture disturbances and overall argue that this experiment has shown a strong indication of future success in employing this method in an operational setting for automated ionospheric detection.

The Mw 7.7 earthquake event showed minimal evidence of coseismic ionospheric disturbance given the station selection, limited by the GUARDIAN network, and local time of event. Therefore we argue that given the data set geometry, detrending method, and timing of the earthquake, the visibility of a disturbance in the ionosphere would be limited in our data and therefore unlikely to be detected given any detection method tested.

Discussion

We note that the magnitude 7.8 local night-time earthquake did not get autonomously detected by the LSTM framework, while it may have been visible to a trained human observer looking at TEC time series for an atmospheric wave disturbance in the range of eight to twelve minutes after a seismic event (Fig. 5). We attribute this miss to variety of factors including time of day (leading to bad signal-to-noise ratios), mechanism of slip, and TEC detrending method used. This shows how dependent this detection method is on uncontrollable factors as well as dataset features. Additionally, three large atmospheric wave disturbances after the magnitude 7.5 local day-time earthquake seen in three signals, BSHM-R805, BSHM-GPS53, and NICO-219 M, Fig. 5, were not detected as anomalous, while their amplitude and phase look similar to the three signals that did result in a positive detection. We believe that these misses are likely due to the sensitivity of the settings for error count and phase synchrony. We argue that error thresholding should be based on a three standard deviation value set by the training data to standardize the definition of anomalous per station-satellite model. In future work we plan to test this detection method without the phase synchrony filter, which contributes to the removal of anomaly detection by the error thresholding and error count filter alone.

Conclusion

In our work, we have utilized TEC data recorded in NRT by the GUARDIAN system as-is (without further processing). We simulated NRT operation by supplying data to our LSTM-based anomaly detection engine in 10-min snippets and demonstrated the successful detection of earthquake-generated TIDs. To the best of our knowledge, this contribution describes the first demonstration of a NRT detection of a geophysical event in a NRT GNSS-based TEC data stream. Unique challenges introduced by the use of the NRT stream are well-represented in our results. We note the existence of detection of signal loss

in our results—these will invariably arise in NRT monitoring, and suggest the need for contextual data from other measurement sources to confirm “true” anomalies from unphysical ones. Seismometers that operate as part of the global seismic monitoring regime remain perhaps the most reliable way to detect earthquakes, primarily because of the high velocity of seismic waves and the incompressible delay atmospheric waves suffer before reaching the ionosphere. Our results presented here serve as a proof of concept that ionospheric anomalies can actually be autonomously flagged, pending the analysis of a subject matter expert in real time. This result becomes particularly interesting when applied to the case of tsunami-induced TIDs, where GNSS networks can augment ocean-buoys in areas of poor coverage. Here, seismometer networks can supply much needed context data about the presence of an earthquake, but GNSS-based ionospheric monitoring has the most added value as it becomes a crucial method able to more directly invert for tsunami parameters (Martire et al. 2022). We acknowledge that this paper uses a continental earthquake event as a test case to determine the feasibility of using ionospheric monitoring as indirect monitoring of natural hazard events on the ground. We plan to continue testing on more natural hazard events, especially on (much rarer) tsunami events, in future work to prove feasibility as a proposed support to ocean monitoring. Thus, there is potential for improvement in the implementation of this

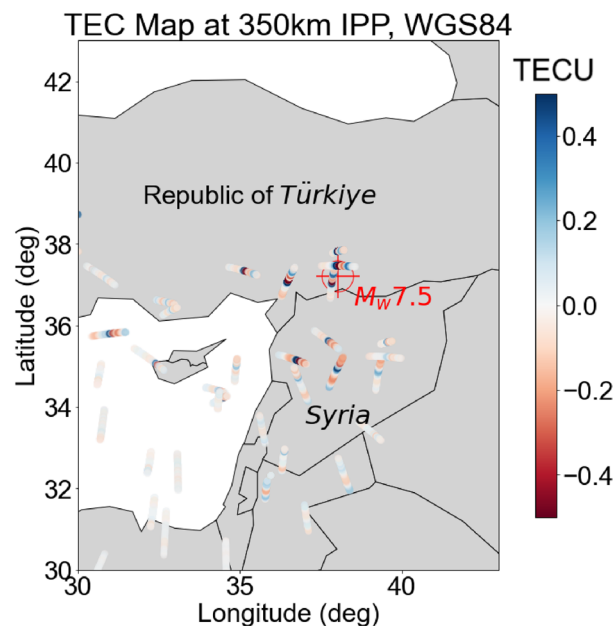


Fig. 8 Ionospheric Pierce Points during 2023-02-06 10:25 to 10:45 UTC, showing the available line-of-sight signals that would be able to detect the atmospheric wave from the seismic event. The $M_w 7.5$ earthquake epicenter is shown with the red cross. This image illustrates the limited coverage during the event from the nearby stations

technique, through better training to avoid non-ionospheric anomalies, more nuanced training on non-anomalous TEC datasets, and frameworks to ingest context data provided by other measurement modalities.

This work represents the use of a relatively sparse dataset in detection of a co-seismic ionospheric disturbance. In this context, sparse refers to the use of only TEC measurements from GNSS signals across a limited amount of stations. This can be fully appreciated by viewing the ionospheric pierce point (IPP) map in Fig. 8 and the limited coverage over the region. From solely TEC measurements we can identify ionospheric behavior of interest. This is an important feature for a deployment of NRT detection in sparse GNSS network regions such as Pacific Island Countries. Our method is in contrast to previous studies that rely on dense GNSS networks for detection such as Maletckii and Astafyeva (2021). Dense networks and "clean", post-processed after-the-fact data, is not available in NRT for hazard warning.

The GUARDIAN system currently tracks approximately 90 stations around the world with significant promise for further growth. Each station typically tracks multiple constellations leading to 60–100 links tracked every day per station. Thus, there is a large volume of data that a human operator must examine to identify subtle ionospheric anomalies following any geophysical event of interest (such as a geomagnetic storm, earthquakes, tsunamis, and volcanic eruptions). Anomalous behavior is intentionally a broad area, defined simply as behavior that is not typically observed in TEC measurements derived from line-of-sight GNSS signals. With our demonstration we have shown the potential that an automated anomaly detection algorithm can provide to significantly reduce the amount of data a human must review to observe these phenomena.

In summary, the ionospheric anomaly detection tool has shown to be novel and robust in several aspects. First, the ability to detect a seismically induced atmospheric waves from two months of slant TEC measurements. Second, unlike previously published TEC anomaly identification techniques, the ability to detect in a near real time scenario, using GUARDIAN TEC data. This data is not post-processed and exhibits the real-life scenario of using real time TEC data streams. Third, the ability to detect anomalies without the use of a dense array of GNSS station data. Our method detected the co-seismic ionospheric disturbance from a single station and three satellites out of 734 station-satellite signals.

Open research

- GUARDIAN TEC and IPP data provided by NASA Crustal Dynamics Data Information System (CDDIS) at https://cddis.nasa.gov/Data_and_Derived_Products/GNSS/Guardian_IonoTEC_001.html

- Python code, ipynb Jupyter Notebook files, and data, csv files, are available on Zenodo at <https://doi.org/10.5281/zenodo.10895878>. Cite as: fionaluhmann. (2023). fionaluhmann/Iono_Anomaly_2023: Ionospheric Anomaly Detection, Kahramanmaraş Earthquake Sequence (v1.0.0). Zenodo. <https://doi.org/10.5281/zenodo.10895878>
- Pytorch was used to develop, train, and test the LSTM neural network (Paszke et al. 2019).
- Continuous Wavelet Transforms by Scipy's Signal CWT function.
- Figures were made with Matplotlib version 3.2.1 (Caswell et al., 2020; Hunter, 2007), available under the Matplotlib license at <https://matplotlib.org/>.
- Maps were created through ArcGIS Pro.

Supplementary Information The online version contains supplementary material available at <https://doi.org/10.1007/s10291-024-01808-2>.

Acknowledgements The authors express their respect and condolences to those who lost loved ones in this earthquake event. Part of this research was carried out with the Jet Propulsion Laboratory, California Institute of Technology under a contract with the National Aeronautics and Space Administration (80NM0018D0004).

Declarations

Conflict of interest The authors have no conflict of interest to declare that are relevant to the content of this article.

Open Access This article is licensed under a Creative Commons Attribution-NonCommercial-NoDerivatives 4.0 International License, which permits any non-commercial use, sharing, distribution and reproduction in any medium or format, as long as you give appropriate credit to the original author(s) and the source, provide a link to the Creative Commons licence, and indicate if you modified the licensed material. You do not have permission under this licence to share adapted material derived from this article or parts of it. The images or other third party material in this article are included in the article's Creative Commons licence, unless indicated otherwise in a credit line to the material. If material is not included in the article's Creative Commons licence and your intended use is not permitted by statutory regulation or exceeds the permitted use, you will need to obtain permission directly from the copyright holder. To view a copy of this licence, visit <http://creativecommons.org/licenses/by-nc-nd/4.0/>.

References

- Afraimovich E, Altynsev A, Grechnev V, Leonovich L (2001) Ionospheric effects of the solar flares as deduced from global GPS network data. *Adv Space Res* 27(6):1333–1338
- Akhoondzadeh M (2013) A MLP neural network as an investigator of TEC time series to detect seismo-ionospheric anomalies. *Adv Space Res* 51(11):2048–2057
- Bagiya MS, Heki K, Gahalaut VK (2023) Anisotropy of the near-field coseismic ionospheric perturbation amplitudes reflecting the source process: the 2023 February Turkey earthquakes.

- Geophys. Res. Lett. 50(14):e2023GL103931. <https://doi.org/10.1029/2023GL103931>
- Brissaud Q, Astafyeva E (2022) Near-real-time detection of co-seismic ionospheric disturbances using machine learning. *Geophys. J. Int.* 230(3):2117–2130
- Calais E, Minster JB (1995) GPS detection of ionospheric perturbations following the January 17, 1994, Northridge earthquake. *Geophys. Res. Lett.* 22(9):1045–1048
- Constantinou V, Ravanelli M, Hamlin L, Bortnik J (2023) Deep learning driven detection of tsunami related internal gravity-waves: a path towards open-ocean natural hazards detection. [arXiv.org](https://arxiv.org/)
- DasGupta A, Das A, Hui D, Bandyopadhyay K, Sivaraman M (2006) Ionospheric perturbations observed by the GPS following the December 26th, 2004 Sumatra–Andaman earthquake. *Earth Planets Space* 58(2):167–172
- Gokceoglu C (2023) 6 February 2023 Kahramanmaraş – Türkiye earthquakes: a general overview. International archives of the photogrammetry, remote sensing and spatial information sciences. (Vol. XLVIII-M-1-2023, pp. 417–424). Gottingen: Copernicus GmbH
- Goldberg DE, Taymaz T, Reitman NG, Hatem AE, Yolsal-Çevikbilen S, Barnhart WD, Altuntaş C (2023) Rapid characterization of the February 2023 Kahramanmaraş, Türkiye, earthquake sequence. *Seismic Rec.* 3(2):156–167
- He H, Queen O, Koker T, Cuevas C, Tsilgkaridis T, Zitnik M (2023) Domain adaptation for time series under feature and label shifts. [arXiv \(Cornell University\)](https://arxiv.org/)
- Hochreiter S, Schmidhuber J (1997) Long short-term memory. *Neural Comput* 9(8):1735–1780
- Hussain E, Kalaycioglu S, Milliner CWD, Cakir Z (2023) Preconditioning the 2023 Kahramanmaraş (Turkiye) earthquake disaster. *Nat Rev Earth Environ* 4(5):287–289
- Kherani EA, Lognonné P, Kamath N, Crespon F, Garcia R (2009) Response of the ionosphere to the seismic triggered acoustic waves: electron density and electromagnetic fluctuations. *Geophys J Int* 176(1):1–13
- Kingma DP, Ba J (2014) Adam: a method for stochastic optimization. *Kotsarenko N, Enriquez R, Koshevaya S (1997) Excitation of plasma waves in the ionosphere caused by atmospheric acoustic waves. Astrophys Space Sci* 246(2):211–217
- Liaw R, Liang E, Nishihara R, Moritz P, Gonzalez JE, Stoica I (2018) Tune: a research platform for distributed model selection and training. [arXiv preprint arXiv:1807.05118](https://arxiv.org/abs/1807.05118)
- Lin J-W (2012) Nonlinear principal component analysis in the detection of ionospheric electron content anomalies related to a deep earthquake (300 km, m 7.0) on 1 January 2012, Izu islands, Japan: Nonlinear principal component analysis. *J Geophys Res Space Phys* 117(A6)
- Liu Y, Morton YJ (2020) Automatic detection of ionospheric scintillation-like GNSS satellite oscillator anomaly using a machine-learning algorithm. *Navigation (Washington)* 67(3):651–662
- Liu Y, Morton YJ (2022) Improved automatic detection of GPS satellite oscillator anomaly using a machine learning algorithm. *Navigation (Washington)* 69(1):navi.500
- Maletckii B, Astafyeva E (2021) Determining spatio-temporal characteristics of coseismic travelling ionospheric disturbances (CTID) in near real-time. *Sci Rep* 11(1):20783–20783
- Maletckii B, Astafyeva E, Sanchez SA, Kherani EA, de Paula ER (2023) The 6 February 2023 Turkiye earthquake sequence as detected in the ionosphere. *J Geophys Res Space Phys* 128(9):e2023JA031663
- Martire L, Krishnamoorthy S, Vergados P, Romans LJ, Szilágyi B, Meng X, Bar-Sever YE (2022) The guardian system—a GNSS upper atmospheric real-time disaster information and alert network. *GPS Solut* 27(1):1521–1886. <https://doi.org/10.1002/jgra.50322>
- Matoba RS, Fee D, Assink JD, Iezzi AM, Green DN, Kim K, Wilson DC (2022) Atmospheric waves and global seismoacoustic observations of the January 2022 Hunga eruption, Tonga. *Science (Am Assoc Adv Sci)* 377(6601):95–100
- Muhammad A, Külahçı F (2022) A semi-supervised total electron content anomaly detection method using LSTM-auto-encoder. *J Atmos Solar-terr Phys* 241:105979
- NGDC, WDS (2023) NCEI/WDS global significant earthquake database, access date 10/09/20243. NCEI/WDS Global Significant Earthquake Database. <https://doi.org/10.7289/V5TD9V7K>
- Occipinti G, Rolland L, Lognonné P, Watada S (2013) From Sumatra 2004 to Tohoku-oki 2011: the systematic GPS detection of the ionospheric signature induced by tsunamigenic earthquakes. *J Geophys Res Space Phys* 118(6):3626–3636. <https://doi.org/10.1002/jgra.50322>
- Okuwaki R, Yagi Y, Taymaz T, Hicks SP (2023) Multi-scale rupture growth with alternating directions in a complex fault network during the 2023 south-eastern Türkiye and Syria earthquake doublet. *Geophys Res Lett* 50(12):e2023GL103480
- Paszke A, Gross S, Massa F, Lerer A, Bradbury J, Chanan G, Chintala S (2019) Pytorch: an imperative style, high-performance deep learning library. In: Wallach H, Larochelle H, Beygelzimer A, d’Alché-Buc F, Fox E, Garnett R (eds) Advances in neural information processing systems. Curran Associates, Inc, vol 32, pp 8024–8035. <http://papers.neurips.cc/paper/9015-pytorch-an-imperative-style-high-performance-deep-learning-library.pdf>
- Riabova SA, Olshanskaya EV, Shalimov SL (2023) Response of the lower and upper ionosphere to earthquakes in Turkey on February 6, 2023. *Izvestiya. Phys Solid Earth* 59(6):957–966
- Rolland LM, Lognonné P, Astafyeva E, Kherani EA, Kobayashi N, Mann M, Munekane H (2011) The resonant response of the ionosphere imaged after the 2011 off the pacific coast of Tohoku earthquake. *Earth Planets Space* 63(7):853–857
- Sak H, Senior A, Beaufays F (2014) Long short-term memory based recurrent neural network architectures for large vocabulary speech recognition. [arXiv \(Cornell University\)](https://arxiv.org/)
- Sanchez SA, Kherani EA, Astafyeva E, de Paula ER (2022) Ionospheric disturbances observed following the ridgecrest earthquake of 4 July 2019 in California, USA. *Remote Sensing* 14(1):188
- Srivastava S, Chandran A, Manta F, Taisne B (2021) GNSS TEC-based detection and analysis of acoustic-gravity waves from the 2012 Sumatra double earthquake sequence. *J Geophys Res Space Phys* 126(6):e2020JA028507
- Teunissen P, Montenbruck O (2017) Springer Handbook of Global Navigation Satellite Systems (First edition), 2017th edn. Springer, Cham
- Zaslavski Y, Parrot M, Blanc E (1998) Analysis of TEC measurements above active seismic regions. *Phys Earth Planet Interiors* 105(3–4):219–228

Publisher's Note Springer Nature remains neutral with regard to jurisdictional claims in published maps and institutional affiliations.